Deposition temperature controlled interfacial degradation of a-C/Cr coatings for 316Lss bipolar plates in PEMFCs

Hao Li [a], Peng Guo [a,*], Keiji Komatsu [c], Guanshui Ma [a], Rende Chen [a], Peiling Ke [a,b], Hidetoshi Saito [a,c], Aiying Wang [a,b,**]

[a] Key Laboratory of Advanced Marine Materials, Ningbo Institute of Materials Technology and Engineering, Chinese Academy of Sciences, 315201, Ningbo, PR China
[b] Centre of Materials Science and Optoelectronics Engineering, University of Chinese Academy of Sciences, 100049, Beijing, PR China
[c] Graduate School of Engineering, Nagaoka University of Technology, 940-2188, Nagaoka, Japan

ARTICLE INFO

ABSTRACT

In proton exchange membrane fuel cells (PEMFCs), the interfacial contact resistance (ICR) of amorphous carbon (a-C) coated metallic bipolar plates (BPs) increased with the passage of time, thereby severely limiting their widespread application. The performance of a-C coated BPs was considerably influenced by interface-induced degradation, which in turn was highly sensitive to sp^2/sp^3, size of sp^2 clusters, and compactness of a-C. These factors were closely linked to the underlying metal transition layers and dependent on the deposition temperature. Therefore, in order to elucidate the impact of interface structure on their performance, a series of a-C coatings with Cr transition layer were magnetron sputtered onto 316L stainless steel at temperatures ranging from room temperature (R.T.) to 400 °C. The results revealed that as the deposition temperature increased, the a-C coatings became more porous and exhibited columnar growth characteristics attributed to the hill-like interface structures of the Cr transition layer. Additionally, both the sp^2 content and cluster size of a-C increased. Correspondingly, the initial ICR decreased from 2.89 Ω cm^2 at R.T. to 1.62 Ω cm^2 at 400 °C. Furthermore, in long-term corrosion tests, both the ICR after corrosion and metal ion concentrations in the corrosion solution rose rapidly. Notably, the a-C coating deposited at 100 °C showed the lowest corrosion current density of 5.81×10^{-4} μA/cm^2 and the smallest increase rate (65.9%) of ICR after the long-term electrochemical corrosion test, owing to its high sp^2 content and dense structure.

1. Introduction

In recent years, proton exchange membrane fuel cell (PEMFC) technologies have become increasingly appealing as a source of clean energy, aimed at addressing the challenges posed by the global energy crisis and environmental pollution [1–3]. In particular, numerous endeavors have highlighted the most promising potential of PEMFC in transportation sectors such as automobiles [4–6], owing to their remarkable power density, swift start-up, low operating temperature, and facile mass production [7,8]. Serving as one of the fundamental constituents within PEMFC systems, bipolar plates (BPs) not only act as conduits for electrical current between cells but also serve as suppliers of reactant gases for both the anode and cathode, as well as facilitators of water and thermal management across cells. It is commonly recognized that BPs account for more than 70% of the overall weight and nearly 50% of the total cost of a single PEMFC stack. In contrast to the graphite and composite materials conventionally employed for BP fabrication, metallic BPs have garnered global attention due to their unparalleled electrical and thermal conductivity, exceptional mechanical properties, and cost-effective processing capabilities [9–11]. Nonetheless, in the presence of temperatures ranging from 60 °C to 80 °C and exceptionally acidic surroundings of pH = 2–3, BPs are susceptible to degradation due to formidable electrochemical or chemical corrosive influences [12,13]. Consequently, this compromises the enduring operational efficacy of PEMFC systems utilized in extensive vehicular applications [14–16].

Protective coatings have been widely recognized as a popular technique for enhancing the electrical conductivity and corrosion resistance of BPs [17,18]. Specifically, metallic noble [19], nitrogen-based [20,

21], carbon-based [22–25], and the latest MAX-phase coatings have emerged as common approaches [26,27]. Among these candidates, noble metallic coatings exhibit superior performance, albeit the expense of their cost is exorbitant. On the other hand, nitrogen-based coatings, fabricated through diverse physical vapor deposition (PVD) methods such as cathodic arc and magnetron sputtering, manifest the synergistic advantages of short-term corrosion resistance combined with exceptional uniformity. However, as a consequence of the corroded metallic elements emanating from defects within the columnar structure of the coating, an increase in interfacial contact resistance (ICR) transpires during prolonged utilization [20,28]. MAX-phase coatings are a particular type of nano-laminated ternary materials possessing a hexagonal structure. The extraordinary layered arrangement of MAX phase coatings grants them exceptional properties derived from both metallics and ceramics. These include superb thermal and electric conductivity, remarkable chemical stability, and a high degree of damage tolerance. Nonetheless, the synthesis of high-purity MAX phase coatings poses various obstacles, such as the requirement for high-temperature (400–900 °C) treatments and a limited window for phase formation. In comparison, amorphous carbon (a-C) coatings, including diamond-like carbon and graphite-like carbon, present a highly promising alternative for achieving both low ICR and anti-corrosion properties in BPs [29,30]. And we found that a-C was more prone to maintaining long-term corrosion resistance in the operating environment of PEMFCs at varying temperatures [31]. Notably, nevertheless, the potentiostatic test demonstrated a pronounced escalation of ICR resulting from the degradation at the interface between a-C and commonly utilized metallic transition layers [32,33]. Wu et al. [34], for instance, employed a pulsed bias arc ion plating technique to deposit Cr doped a-C coating on 316L stainless steel (316Lss). They discovered that the ICR of coatings exhibited no less than a twofold increase compared to its pristine counterpart following a 7 h potentiostatic test in both simulated cathodic and anodic environments. This phenomenon was attributed to the occurrence of pitting corrosion induced by pinholes or defects during the growth of the coating. A similar outcome could be observed in pure a-C coatings [35]. As an alternative approach to diminishing the initial ICR of a-C coatings, a preference was given to larger-sized sp^2 clusters and a greater abundance of hexagonal carbon rings [32]. Furthermore, it was significantly observed that the ICR and corrosion resistance of a-C-coated BPs were strongly reliant on the ratio of sp^2/sp^3, the size of sp^2 clusters, and the compactness of a-C coating growth [36]. However, it is noteworthy that despite the excellent physical and chemical properties offered by a-C coating technology, the degradation mechanism of a-C coated BPs remains a contentious subject that requires further elucidation.

In our previous work, we successfully fabricated a hydrogen-free a-C coating on 316Lss using the direct current magnetron sputtering (DCMS) [32,37]. Notably, we employed X-ray reflectivity (XRR) to assess the changes in compactness of the a-C coating before and after a 12 h electrochemical test. The results demonstrated that degradation at the interface was the primary factor contributing to the increased ICR and deterioration of the corrosion resistance of the a-C coating in a simulated PEMFC environment [35,38].

Therefore, considering the proposed structural zone diagram (SZD) for controlling the deposition temperature, it is crucial to explore the impact of temperature on the microstructure of the top a-C coating and Cr transition buffer-layer. These factors play a crucial role in determining the long-term protective performance of the coated BPs in acidic environments for PEMFCs [36]. However, the impact of deposition temperature on the protective performance of coated BPs has not yet been thoroughly investigated.

For this purpose, we synthesized a series of a-C coatings on 316Lss using the DCMS technique, with varying deposition temperatures ranging from 25 to 400 °C. Concurrently, a Cr layer was employed as a transitional buffer-layer to enhance the adhesion between the a-C coating and the substrate. It is noteworthy that Cr possesses a more

potent catalytic effect on the interfacial graphitization of a-C, thereby augmenting the carrier transfer required for adequate electrical conductivity [39,40]. Subsequently, the corrosion resistance and ICR of the Cr/a-C-coated 316Lss were evaluated before and after a 12 h electrochemical corrosion test. The underlying degradation mechanism was elucidated based on the evolution of the interfacial structure and the concentration of metallic ions dissolved in the acidic solution.

2. Experimental details

2.1. Coating deposition

All of the coatings were fabricated by DCMS, in accordance with our previously published report [32,35]. The target materials and the fabrication procedure followed the guidelines provided in Refs. [32,37]. For the ICR and corrosion tests, 0.1 mm thick 316Lss substrates were employed. Additionally, P-type Silicon (100) wafers were simultaneously utilized for microstructural analysis and mechanical characterization of the prepared a-C coatings. To enhance adhesion strength, a Cr transition layer was first deposited. Subsequently, the a-C coatings were deposited at various temperatures: room temperature (R.T.), 100 °C, 200 °C, 300 °C, and 400 °C. The thickness of all the a-C films was carefully controlled to be around 200 nm by precise regulation of the deposition time. For more detailed parameters, please refer to our previous publication.

2.2. Structural characterization

The surface and cross-sectional morphologies of the coatings were assessed through thermal field emission scanning electron microscopy (SEM, Verios G4 UC, Thermo scientific, US). The roughness was evaluated using atomic force microscopy (AFM, Dimension 3100, Vecco, US) in tapping mode, employing a 5 μm × 5 μm test area. The structure of a-C was characterized utilizing Raman spectra (Renishaw inVia Reflex, UK) with a wavelength of 532 nm and a scanning range of 800–2000 cm^{-1}. For the analysis of sp^3/sp^2 contents before and after corrosion tests, X-ray photoelectron spectroscopy (XPS, Axis Ultra DLD, Kratos, UK) was employed, using monochromatic Al Kα irradiation with a pass energy of 160 eV. No pre-treatment was employed to maintain the initial surface. Transmission electron microscopy (TEM, Tecnai F20, FEI, US) was conducted to investigate the microstructure of the coatings, wherein the milling process was performed using focused ion beam (FIB, Auriga, Carl Zeiss, GER) with a Ga ion source. To elucidate the alterations in carbon bonding, scanning transmission electron microscopy (STEM) was employed for the observation of electron energy loss spectroscopy (EELS), where highly oriented pyrolytic graphite (HOPG) served as the reference for analyzing the sp^2-C content. The coating density was measured using X-ray reflectivity (XRR) with a Cu Kα radiation source at a wavelength of 1.54 Å, wherein the incident angle was varied within the range of 0.2–2.5° with a scanning increment of 0.004°. The reflection intensity was obtained using an X-ray diffraction apparatus (M03XHFMXP3, MacScience). Following Parratt's theory, the XRR profiles were simulated using GXRR software, which is a commercial software package dedicated to analysis purposes [41–43].

2.3. Electrochemical and conductive test

The electrochemical three electrode system was employed to assess the corrosion resistance of the a-C coated 316Lss. The fabricated coatings operated as the working electrode, while the platinum electrode served as the counter electrode and the Ag/AgCl was utilized as the reference electrode. In accordance with the technical standard set by the US Department of Energy (DOE), the test specimen underwent scanning between −0.3 V and 1.5 V (vs. Ag/AgCl) in an electrolyte solution with a pH = 3, consisting of H$_2$SO$_4$ and 0.1 ppm HF, at a temperature of 80 °C. The scan rate employed was 0.5 mV/s [44–46]. To evaluate the
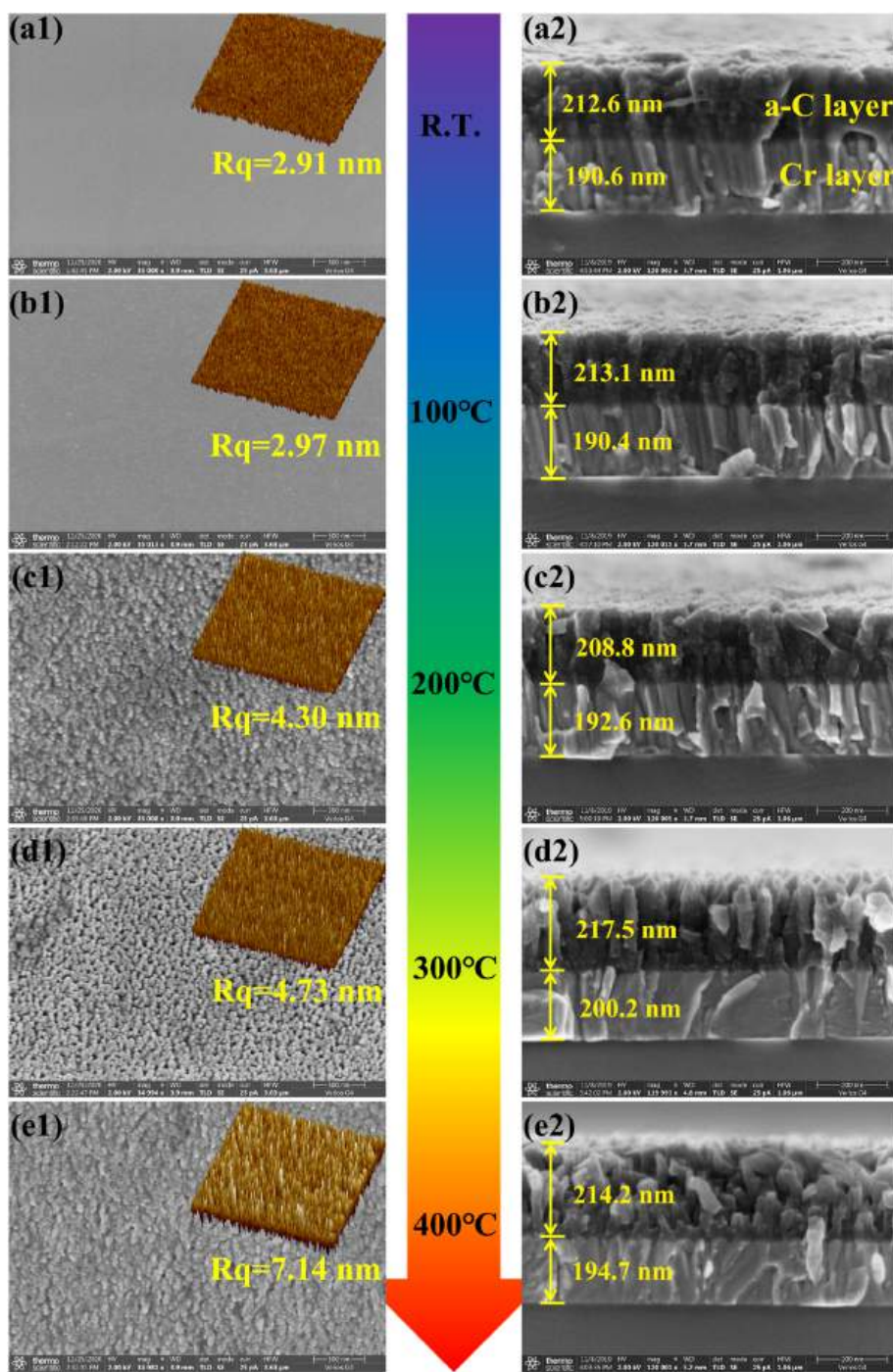
Fig. 1. SEM images of surface and cross-sectional morphology of a-C coatings deposited at (a) R. T., (b) 100 °C, (c) 200 °C, (d) 300 °C, (e) and 400 °C; The inserted figures in (a1-e1) are the AFM surface topographies.

corrosion stability of the coating in a simulated PEMFC cathode environment, the potential of the working electrode was maintained at a constant value of 0.6 V vs. Ag/AgCl during potentiostatic polarization tests lasting 12 h. The electrochemical impedance spectroscopy (EIS) technique was used to evaluate the corrosion properties of all the coated 316Lss in simulated PEMFC solution. The EIS measurements were recorded at OCP in the frequency range of 10^5 to 10^{-2} Hz with 10 mV sinusoidal perturbation. Prior to initiating all corrosion tests, an open circuit potential (OCP) measurement was conducted for a duration of 60 min. The surface area exposed during all electrochemical assessments is 1 cm² for the specimens. Once the OCP had gradually stabilized, the corresponding scanning procedure was subsequently performed.

Following the potentiostatic test, 20 mL of acidic solution was collected for characterization using inductively-coupled plasma optical emission spectroscopy (ICP-OES, SPECTRO ARCOSII, GER).

The ICR of the coating was quantified using the technique proposed by Davies et al. [47,48]. In this method, two sheets of carbon paper (Toray TGP-H-060) were placed between two copper plates coated with gold. The coated specimen was then subjected to a pressure of 1.38 MPa. To measure the voltage variation across the entire circuit at different pressures, a sophisticated multimeter equipped with a constant current power supply and an external 1 A circuit was utilized. The circuit resistance was subsequently determined through voltammetry calculations.
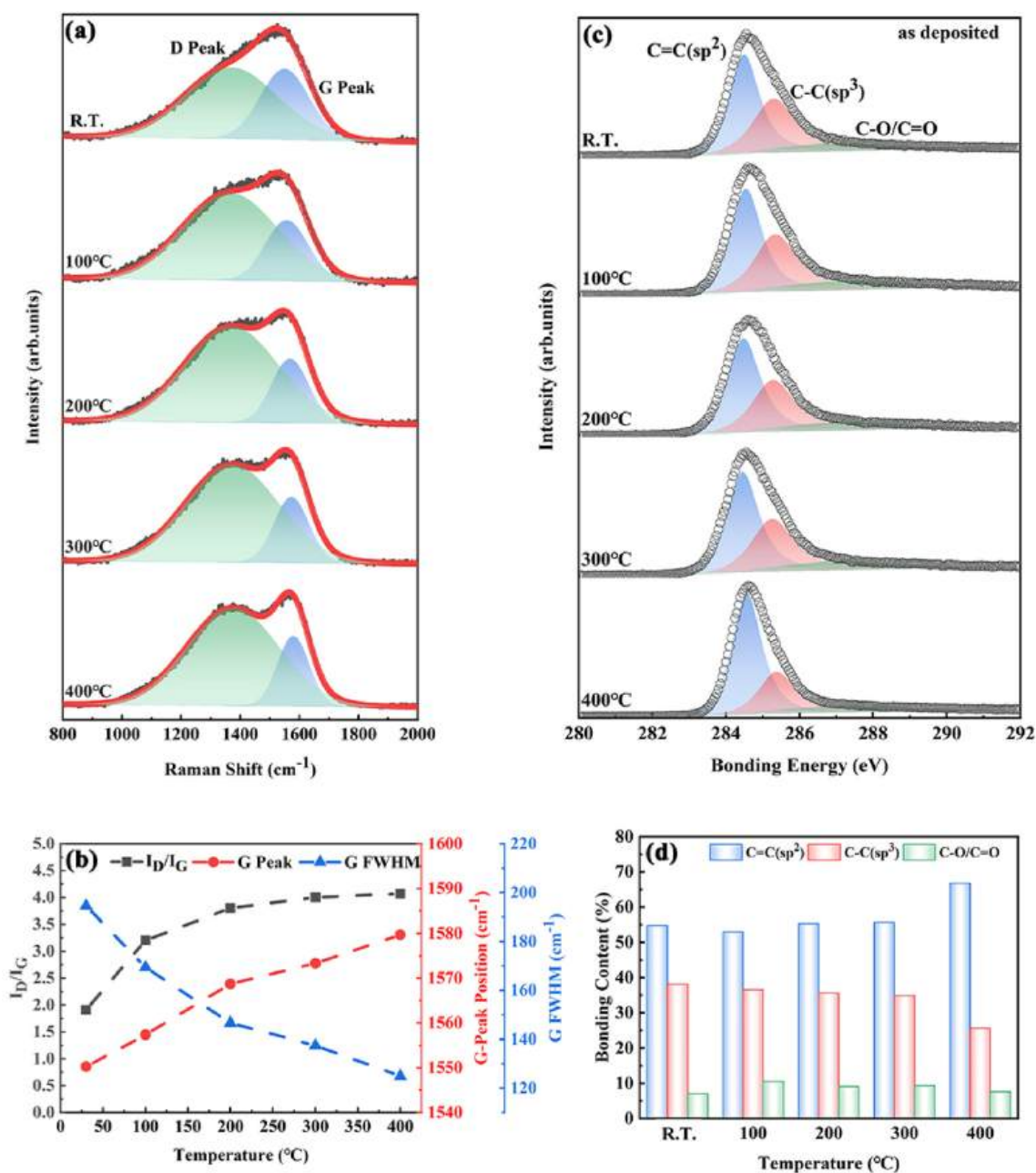
Fig. 2. (a) Raman spectra and (b) corresponding I_D/I_G ratio, G peak position and G FWHM of the a-C coatings; (c) XPS C 1s core level spectra and (d) corresponding sp^2, sp^3 and C–O/C=O contents of the a-C coatings.

3. Results and discussion

3.1. Morphology of Cr/a-C coatings

Fig. 1 illustrates the surface and cross-sectional morphology of the coatings deposited at various temperatures. As depicted in Fig. 1(a1-e1), as the temperature increased from R. T. to 400 °C, the coating surface became textured, with an increased presence of cauliflower-like structures. This can be attributed to the accelerated growth rate of sp^2 clusters at higher temperatures, potentially catalyzed by the underlying metallic layer [35,39,49,50]. The corresponding AFM analysis inserted in the Fig.1 further corroborates these observations, unveiling a gradual increase in surface roughness (Rq) from 2.91 nm at R. T. to 7.14 nm at 400 °C.

Moreover, the cross-sectional morphology in Fig. 1(a2-e2) exhibited a bilayer structure for all samples, with a controlled Cr layer thickness of approximately 195 ± 10 nm and a-C layer thickness around 210 ± 10 nm. Furthermore, as the temperature increased, particularly beyond 200 °C, the a-C coatings gradually acquired a more porous structure, displaying a columnar growth pattern. This phenomenon arises due to the preference of a-C coatings to grow along the Cr transition layer orientation [50,51].

3.2. Chemical composition of Cr/a-C coatings

Raman spectroscopy serves as a non-destructive technique for elucidating the carbon bond structure of a-C coatings. Fig. 2(a) exhibits the Raman spectra of a-C coatings fabricated at varying temperatures. Each spectrum exhibits two characteristic peaks, namely the D peak and G peak. The D peak, situated at approximately 1350 cm^{-1}, corresponds to the breathing mode of sp^2-C atoms within the ring structure. Conversely, the G peak, found at around 1580 cm^{-1}, corresponds to the
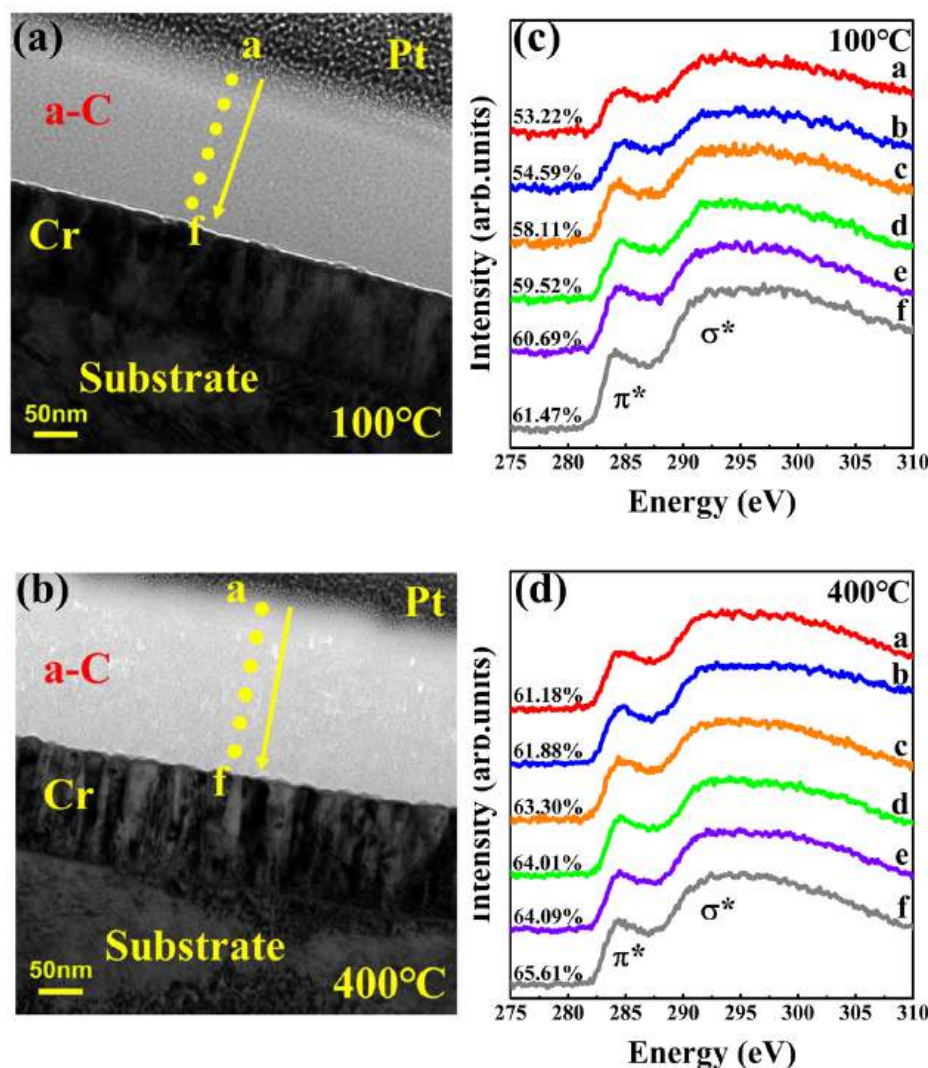
Fig. 3. (a, b) Cross-sectional TEM image of the samples deposited at 100 °C and 400 °C, and (c, d) the C–K edge spectra obtained from different locations labelled as a-f in the TEM image for different EELS position.

stretching mode of sp^2-C atoms [52]. The determined I_D/I_G ratio, peak position, and full width at half maximum (FWHM) can be utilized to analyze the atomic bonds present in a-C coatings. With an increase in temperature from R. T. to 400 °C, the D peak and G peak gradually exhibited a splitting behavior, particularly beyond 300 °C, indicating a pronounced inclination towards graphitization [53]. Simultaneously, the I_D/I_G ratio escalated from 1.91 to 4.07, while the G peak position also elevated from 1550 cm^{-1} to 1580 cm^{-1}, as depicted in Fig. 2(b). This signifies an increased sp^2 content and cluster size [52,54]. Conversely, the FWHM of the G peak diminished from 194.5 cm^{-1} to 124.9 cm^{-1}, thereby suggesting a more organized structure of the a-C coatings [54].

Fig. 2(c) illustrates the XPS spectra of C 1s and the proportions of C=C (sp^2), C–C (sp^3), and C–O/C=O present in the deposited a-C. The presence of oxygen could be attributed to either air adsorption on the sample surface or residual air within the chamber. The relative proportions of different hybrid carbon atoms were determined through a blended Gaussian (20%) and Lorentz (80%) fitting, following the elimination of Shirley background. In Fig. 2(d), it was observed that the proportion of C=C (sp^2) increased from 54.79% to 66.74% as the temperature rises. Notably, at 400 °C, the sp^2 content exhibited a growth of over 20% compared to that at 300 °C (55.70%), consistent with the aforementioned Raman results.

Fig. 3(a, b) exhibit the TEM images of two exemplary samples deposited at 100 °C and 400 °C, correspondingly. The Cr layers showcased prominent columnar crystalline structure, particularly at 400 °C, where numerous hill-like structures measuring around 20–30 nm emerged at the interface. Despite this, all the a-C layers still maintained their amorphous structure, with an evident interface discernible. However, unlike the homogeneous and compact structure of the a-C at 100 °C, certain pinholes or defects could be observed in the a-C deposited at 400 °C, as depicted in Fig. 3(b). In Fig. 3(c and d), EELS was employed to scrutinize the alteration in bond structure from the surface to the interface of the a-C layer, and the designated test positions were marked in Fig. 3(a and b). By executing a fitting procedure on the EELS curve using the two-window method [32,55–57], the concentration of sp^2 was computed as follows,

$$\frac{(S\pi^*/S\sigma^*)_{film}}{(S\pi^*/S\sigma^*)_{standard}} = \frac{3-x}{4x} \tag{1}$$

where $S\pi^*$ and $S\sigma^*$ denote the integral areas of the π^* and σ^* peaks, respectively. At both 100 °C and 400 °C, the sp^2 content in the a-C layer exhibited a monotonic increase from the surface to the interface, a phenomenon commonly attributed to metal catalysis at the interface [49,51]. Specifically, for a-C deposited at 100 °C, the sp^2 content at the surface (53.22%) was significantly lower compared to that at the
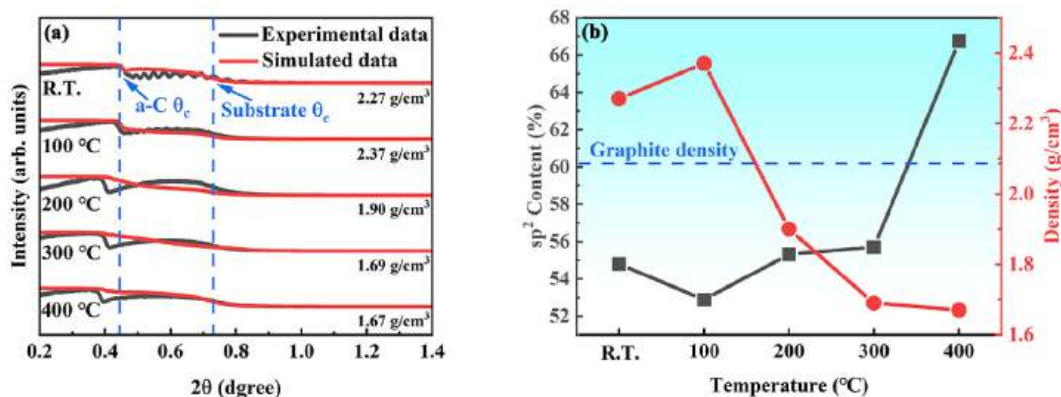
Fig. 4. (a) The X-ray reflectivity data and (b) calculated density for a-C coatings deposited at various temperatures.
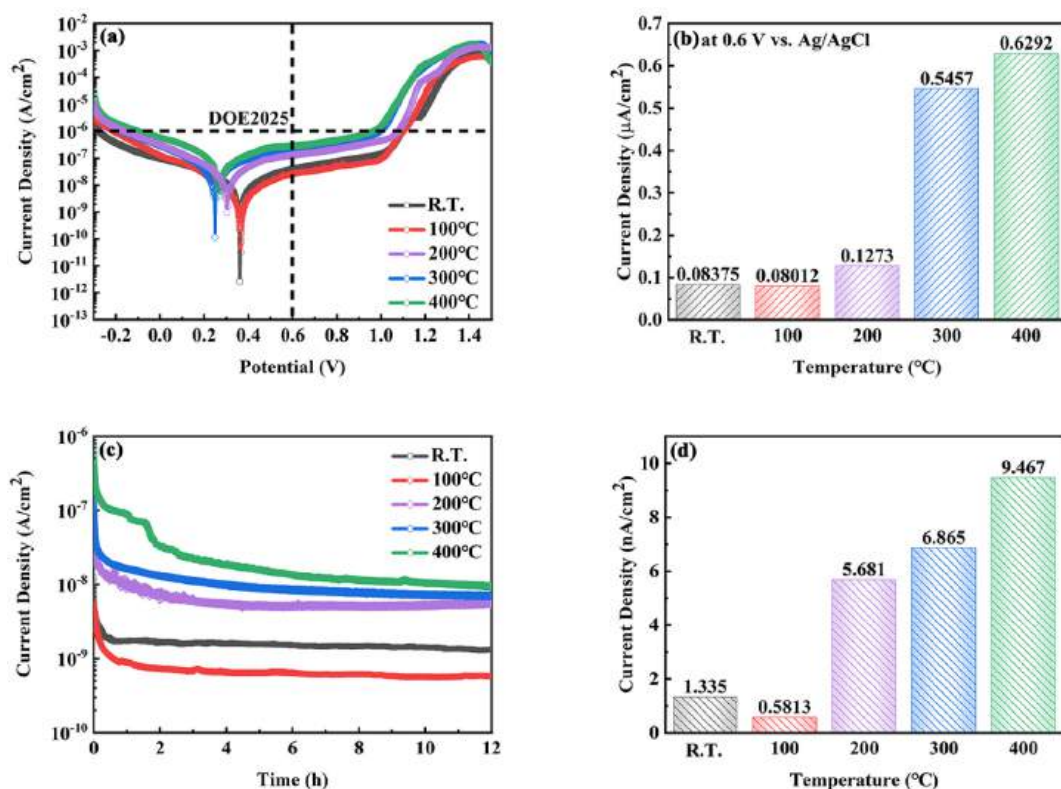

Fig. 5. (a, b) potentiodynamic polarization and (c, d) 0.6 V potentiostatic polarization curves of a-C coatings deposited at different temperature.

interface (61.47%). However, at 400 °C, the corresponding sp² content rose only from 61.18% to 65.61%, due to the graphitization of the surface a-C coatings caused by heightened temperatures [38]. Thus, it can be inferred that metal catalysis predominantly influences the a-C layer near the interface, whereas the surface is primarily affected by graphitization induced by elevated temperatures [35].

In order to expound upon the temperature-dependent density evolution of coatings, additional XRR tests were conducted. Fig. 4(a) depicts the XRR data encompassing an angular range of 0.2–1.4° in 2θ, along with the calculated densities of the a-C layers. XRR, being a non-invasive and efficacious testing technique, enables the determination of the density (ρ) of the a-C layer through the employment of the subsequent formula,

$$\rho = \left[\frac{\pi \theta_c^2}{N_A r_e \lambda^2} \right] \left[\frac{M_C}{Z_C} \right] \tag{2}$$

Where θ_C is the critical angle in radians, r_e is the electron radius, N_A is the Avogadro constant, λ is the wavelength employed by the instrument, Z_C is the numbers of the carbon atom, and M_C is the molar mass of the carbon, respectively [42,54,58–60]. As the temperature rises, the ρ of the a-C layer initially ascends from 2.27 g/cm² to 2.37 g/cm², subsequently declining to 1.67 g/cm² beyond 100 °C. Generally, the density of hydrogen-free a-C predominantly relies on both the defect density and sp²/sp³ ratio [58]. According to XPS analysis, the fluctuation in the sp² content within the a-C coatings was less than 12% (ranging from 54.79% to 66.74%), while the maximum density variation estimated by XRR amounted to approximately 41.9%, as showed in Fig. 4(b). The density of highly crystallized graphite possessing 100% sp² content is no less than 2.09–2.33 g/cm³ [61], the decrease in density of the a-C coatings can be elucidated by the augmented defects or loose structure, aligning with the morphology observed via SEM.
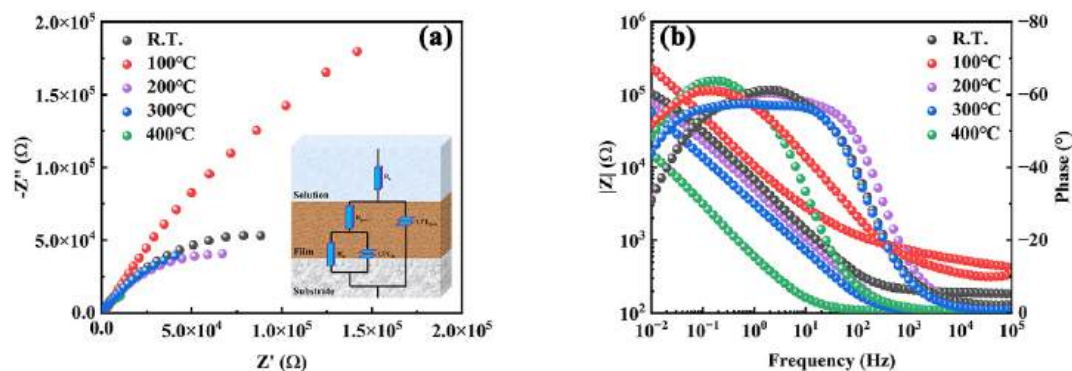
Fig. 6. (a) The Nyquist plots and (b) Bode plots of a-C coatings deposited at different temperature.

Table 1
The EIS fitting results of the specimens.

Temperature (°C)	R_s ($\Omega \cdot cm^2$)	CPE_{pore} ($\mu F/cm^2$)	n_{pore}	R_{pore} ($k\Omega \cdot cm^2$)	CPE_{dl} ($\mu F/cm^2$)	n_{dl}	R_{ct} ($k\Omega \cdot cm^2$)	$\Sigma\chi^2 \times 10^{-4}$
R.T.	104	34.7	0.832	4.60	25.5	0.715	784.6	0.77
100	99.2	35.1	0.827	5.10	29.0	0.728	850.0	0.28
200	99.1	37.2	0.819	3.85	28.4	0.662	472.7	0.32
300	104	38.7	0.875	2.35	28.0	0.676	429.0	3.11
400	99.3	38.4	0.814	3.12	28.0	0.681	420.0	0.38

3.3. Electrochemical and conductive properties

The durability of PEMFCs heavily relies on the corrosion resistance of BPs. To assess this, potentiodynamic polarization curves were conducted for all coated metallic BPs, as depicted in Fig. 5(a). Evidently, each sample met the DOE2025 standard (<1 $\mu A/cm^2$). Notably, the sample deposited at 100 °C exhibited the most favorable corrosion current density, standing at approximately 8.38×10^{-2} $\mu A/cm^2$, at 0.6 V vs. Ag/AgCl, as presented in Fig. 5(b). As the temperature crossed the threshold of 100 °C, the corrosion current density demonstrated an upward trend, proportional to the rise in temperature. The sample prepared at a high deposition temperature of 400 °C exhibited the highest corrosion current density, reaching 0.629 $\mu A/cm^2$.

The 12 h potentiostatic polarization test was conducted at a working potential of 0.6 V vs. Ag/AgCl, as illustrated in Fig. 5(c and d), which represents the typical operational potential for PEMFCs. The findings were consistent with the potentiodynamic polarization test, revealing that the sample exhibited the most outstanding performance at 100 °C in the potentiostatic polarization test, showing a steady corrosion current density of 5.81×10^{-4} $\mu A/cm^2$. As the deposition temperature rose to 400 °C, the corrosion current density increased rapidly, ultimately

reaching its peak value at approximately 9.47×10^{-3} $\mu A/cm^2$.

The EIS technique was employed to investigate the corrosion mechanisms of the a-C coatings deposited at various temperatures. Fig. 6 shows the Nyquist and Bode plots for all samples. The Nyquist plots reveal an initial increase followed by a decrease in the capacitance loop radius as the deposition temperature increases, reaching its maximum value at 100 °C. Likewise, the absolute impedance value at 0.01 Hz ($|Z|_{0.01}$) followed a similar trend, which acts as an indicator of the anti-corrosion performance of the a-C coatings in this study, as depicted in the Bode impedance plots. Based on the Bode plots, the $|Z|_{0.01}$ for the a-C coating deposited at 100 °C measured 228900 Ω cm^2, while for the coating deposited at 400 °C, it dropped significantly to only 56740 Ω cm^2, implying a weaker anti-corrosion ability for this particular sample. Typically, the capacitive response in the low-frequency region indicates the reaction at the interface between the electrolyte and substrate, predominantly occurring at the bottom of defects. Consequently, the sample deposited at 400 °C exhibited a more pronounced presence of defects at the interface.

The ZSimpWin software was employed for the fitting of the EIS, as outlined in Table 1. The equivalent circuit depicted in the inserts of Fig. 6(a) was utilized to characterize the impedance of a-C coated
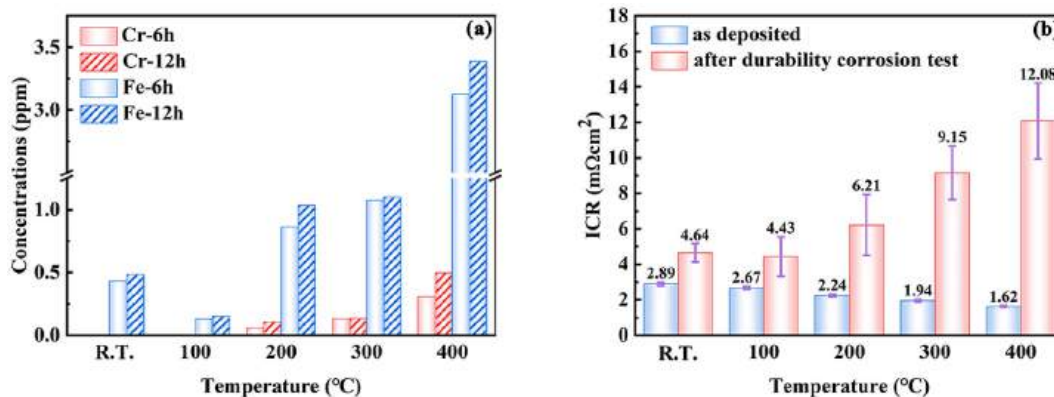

Fig. 7. (a) Concentrations of Fe and Cr ions released from modified 316Lss under simulated PEMFC operational conditions after 6 h and 12 h potentiostatic test, (b) ICR before and after 12 h corrosion tests of a-C modified 316Lss.
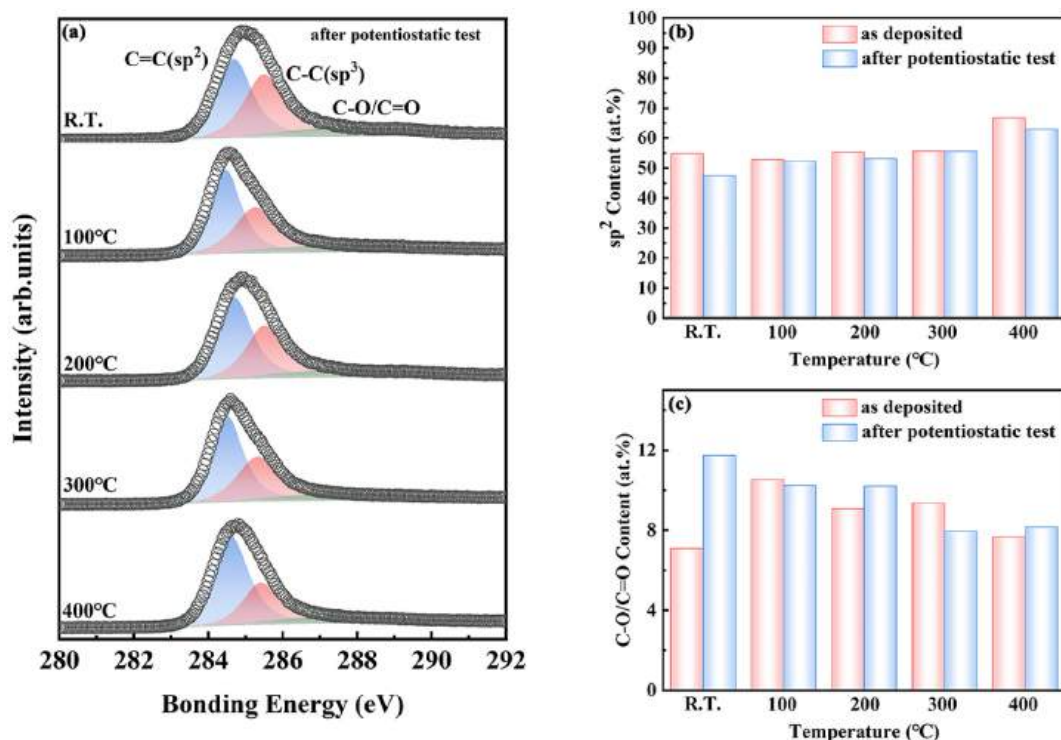
Fig. 8. (a)XPS spectra, (b) sp^2 and (c) C–O/C=O contents after electrochemical corrosion tests of a-C coating deposited at different temperature.

316Lss. The R_s, R_{pore}, and R_{ct} denoted the solution resistance, pore resistance, and charge transfer resistance, respectively. Furthermore, acknowledging the non-uniform nature of the deposited coatings, a Constant Phase Element (CPE) was introduced to account for this imperfect capacitance. The CPE_{pore} and CPE_{dll} represented the coating capacitance and double-layer capacitance, respectively.

With the escalation of deposition temperature, R_{ct} initially increased from 784.6 kΩ cm^2 to 850.0 kΩ cm^2 before declining to 420.0 kΩ cm^2. This trend signified that the charge transfer and corrosion phenomena were more pronounced at the substrate interface, attributed to an abundance of defects and enhanced conductivity within the a-C coating deposited at 400 °C.

In order to assess the effectiveness of the a-C coatings in terms of protection, a 20 mL of the corrosion solution was collected respectively for measuring the concentration of metal ions after 6 h and 12 h corrosion tests. The extent of metal dissolution was inversely related to the corrosion resistance exhibited by the a-C coating. As depicted in Fig. 7(a), notable levels of both Cr and Fe were detected. Notably, the lowest concentrations were observed at a deposition temperature of 100 °C, while the highest values were recorded at 400 °C. At R. T. and 100 °C, the presence of Cr could not be identified, indicating that the two a-C coatings offered exceptional resistance against acid corrosion [62]. Nevertheless, the dissolution of Fe suggested that neither the Cr layer nor the a-C layer can provide complete protection for the metallic BPs. Furthermore, the concentrations of these elements also witnessed an increase over time as the corrosion proceeded. For instance, following a corrosion test conducted over a duration of 12 h, the concentration of Fe in the samples deposited at 400 °C is approximately 3.39 ppm, surpassing its 6 h value of 3.13 ppm. This rise in the concentration of metal ions with test duration indicated continuous corrosion of the substrate.

The ICR before and after the 12 h corrosion test was quantified, as illustrated in Fig. 7(b). Prior to the corrosion test, the a-C coated 316Lss exhibited a steady decline in ICR, ranging from 2.89 Ω cm^2 to 1.62 Ω cm^2, as the deposition temperature increased. Subsequent to the corrosion test, a significant augmentation was observed in the ICR values of all specimens. Intriguingly, the ratio of ICR increase was found

to be inversely correlated with the corrosion resistance of the a-C modified 316Lss. For a-C deposited at 100 °C, the ICR merely experienced a 65.9% elevation, whereas at 400 °C, its ICR increased by nearly sevenfold, reaching 12.08 mΩ cm^2, surpassing even the DOE2025 standard of 10 mΩ cm^2.

3.4. Microstructure characterization after the electrochemical corrosion

XPS was used to analyze the change of carbon bond structure after corrosion, as shown in Fig. 8. Compared with the as-deposited samples, all a-C coatings exhibited the similar carbon bond structure after corrosion test. The sample deposited at higher temperature still had a higher sp^2 content, despite its value decreased slightly, since a minority of weaker C-sp^2 bond may be corroded in the harsh acid electrolyte [63–65]. Similarly, the change of C–O/C=O content was less than 4%, perhaps attributed to the adsorption of liquid or air on the surface during the corrosion test, and no pre-treatment was employed before XPS test to preserve the original surface.

3.5. Discussion

Based on the structural characterization, the deposition temperature exerted a significant influence on the ratio of sp^2/sp^3, the size of sp^2 clusters, the compactness of a-C coatings, and the interface structure between a-C and the Cr transition layer. Primarily, as the deposition temperature increased, both the sp^2 content and the size of sp^2 clusters in the a-C coating experienced substantial growth, attributed to the graphitization of a-C. Simultaneously, as the temperature escalated from 100 °C to 400 °C, the density of the a-C coatings exhibited a monotonic decrease from 2.37 g/cm^2 to 1.67 g/cm^2. Two factors, namely the sp^2/sp^3 ratio and the compactness of the a-C coatings, warrant consideration. On one hand, the elevated temperature and the catalytic effect of the metal transition layer led to a higher sp^2/sp^3 ratio and reduced density of a-C. On the other hand, the a-C layer and the Cr transition layer demonstrated analogous growth patterns, supported by the SEM and TEM cross-sectional morphology. The Cr grains exhibited rapid
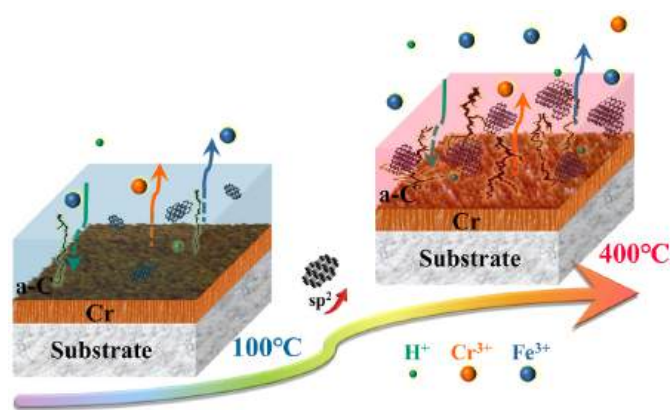
Fig. 9. Interface-induced degradation behaviour of a-C coated bipolar plates deposited at various deposition temperature.

growth with increasing temperature [66]. The presence of hill-like interface structures, resulting from the underlying Cr transition layer, may contribute to more pinholes or defects in the top a-C layer.

After subsequent corrosion resistance evaluation and ICR testing, the initial ICR of the a-C coating declined from 2.89 mΩ cm^2 at R. T. to 1.62 mΩ cm^2 at 400 °C, benefiting from an elevated sp^2 content that imparts enhanced conductivity. However, following the corrosion test, the increase of ICR demonstrated an adverse association with the corrosion resistance of the a-C coatings. The a-C coating with the most compact structure exhibited the lowest corrosion current density (5.81 $\times$ 10^{-4} μA/cm^2) and the lowest increase rate (65.9%) of ICR after corrosion. Albeit the microstructure of all a-C coatings remained stable after corrosion test, the presence of Fe and Cr ions in the corrosion solution signified the severe corrosion of metallic BPs through the occurrence of pinholes and defects in the a-C coatings, as depicted in Fig. 9. Consequently, the a-C coating deposited at 100 °C displayed the least amount of corrosion owing to its densest structure, the lowest ICR resulting from a higher sp^2/sp^3 ratio, and exhibited superior performance during electrochemical corrosion.

4. Conclusion

In this study, we prepared a series of a-C coatings onto 316Lss by DCMS. By increasing the deposition temperature from R. T. to 400 °C, both the content and cluster size of sp^2 carbon in the a-C coatings increased. Consequently, their initial ICR decreased from 2.89 Ω cm^2 at R. T. to 1.62 Ω cm^2 at 400 °C. Furthermore, the loose structure of the a-C coatings, induced by the hill-like interface structures, resulted in more pinholes or defects in the top layer of the coating. After a corrosion test lasting 12 h, the ICR was noticeably increased, alongside a significant increase in the concentration of metal ions in the corrosive solution. It is intriguing that a-C coatings deposited at 100 °C exhibit optimal performance. This can be attributed to the high sp^2 carbon content and the compactness of the coating, which help reduce the initial ICR and minimize the corrosion of metallic BPs during electrochemical corrosion testing. Overall, this study highlights the potential for improving the performance of a-C coated BPs by optimizing the interface structures and compactness of the a-C coatings through temperature adjustment during the deposition process.

Enhancing the density and size of sp^2 clusters concurrently holds the key to crafting a-C coatings boasting superior conductivity and corrosion resistance. With this concept as the foundation, forthcoming advancements in coating growth may involve a more targeted approach, perhaps by manipulating the plasma state throughout the deposition process.

CRediT authorship contribution statement

Hao Li: Writing – review & editing, Writing – original draft, Software, Methodology, Data curation. **Peng Guo:** Supervision, Funding acquisition, Conceptualization. **Keiji Komatsu:** Writing – review & editing, Data curation. **Guanshui Ma:** Writing – review & editing, Data curation. **Rende Chen:** Writing – review & editing, Conceptualization. **Peiling Ke:** Writing – review & editing, Conceptualization. **Hidetoshi Saito:** Writing – review & editing, Conceptualization. **Aiying Wang:** Writing – review & editing, Supervision, Methodology, Funding acquisition, Conceptualization.

Declaration of competing interest

The authors declare that they have no known competing financial interests or personal relationships that could have appeared to influence the work reported in this paper.

References

[1] Wagner FT, Lakshmanan B, Mathias MF. Electrochemistry and the future of the automobile. J Phys Chem Lett 2010;1:2204–19.

[2] Daud WRW, Rosli RE, Majlan EH, Hamid SAA, Mohamed R, Husaini T. PEM fuel cell system control: a review. Renew Energy 2017;113:620–38.

[3] Mohideen MM, Subramanian B, Sun JY, Ge J, Guo H, Radhamani AV, et al. Techno-economic analysis of different shades of renewable and non-renewable energy-based hydrogen for fuel cell electric vehicles. Renewable Sustainable Energy Rev 2023;174.

[4] Asri NF, Husaini T, Sulong A, Majlan EH, Daud WRW. Coating of stainless steel and titanium bipolar plates for anticorrosion in PEMFC: a review. Int J Hydrogen Energy 2017;42:9135–48.

[5] Peng LF, Yi PY, Lai XM. Design and manufacturing of stainless steel bipolar plates for proton exchange membrane fuel cells. Int J Hydrogen Energy 2014;39: 21127–53.

[6] Sharma S, Ghoshal SK. Hydrogen the future transportation fuel: from production to applications. Renewable Sustainable Energy Rev 2015;43:1151–8.

[7] Li XG, Sabir M. Review of bipolar plates in PEM fuel cells: flow-field designs. Int J Hydrogen Energy 2005;30:359–71.

[8] Giddey S, Ciacchi FT, Badwal SPS. Design, assembly and operation of polymer electrolyte membrane fuel cell stacks to 1 kWe capacity. J Power Sources 2004; 125:155–65.

[9] Yi P, Peng L, Zhou T, Wu H, Lai X. Development and characterization of multilayered Cr–C/a-C:Cr film on 316L stainless steel as bipolar plates for proton exchange membrane fuel cells. J Power Sources 2013;230:25–31.

[10] Calebrese C, Eisman GA, Lewis DJ, Schadler LS. Swelling and related mechanical and physical properties of carbon nanofiber filled mesophase pitch for use as a bipolar plate material. Carbon 2010;48:3939–46.

[11] Wenkai L, Zhiyong X, Haodong Z. Current status of research on composite bipolar plates for proton exchange membrane fuel cells (PEMFCs): nanofillers and structure optimization. RSC Adv 2024;14:7172–94.

[12] Choi JH, Kang HE, Kim DJ, Yoon YS. A comprehensive review of stainless-steel bipolar plate coatings and their role in mitigating corrosion in aggressive proton-exchange membrane fuel cells environments. Chem Eng J 2024;493.

[13] Pugal Mani S, Rajendran N. Corrosion and interfacial contact resistance behavior of electrochemically nitrided 316L SS bipolar plates for proton exchange membrane fuel cells. Energy 2017;133:1050–62.

[14] Ehteshami SMM, Taheri A, Chan SH. A review on ions induced contamination of polymer electrolyte membrane fuel cells, poisoning mechanisms and mitigation approaches. J Ind Eng Chem 2016;34:1–8.

[15] Papadias DD, Ahluwalia RK, Thomson JK, Meyer HM, Brady MP, Wang HL, et al. Degradation of SS316L bipolar plates in simulated fuel cell environment: corrosion rate, barrier film formation kinetics and contact resistance. J Power Sources 2015; 273:1237–49.

[16] Weber AZ, Borup RL, Darling RM, Das PK, Dursch TJ, Gu WB, et al. A critical review of modeling transport phenomena in polymer-electrolyte fuel cells. J Electrochem Soc 2014;161:F1254–99.

[17] Kang HE, Choi J-H, Lee U, Kim H-G, Yoon YS. Characterization of CrAl coating on stainless steel bipolar plates for polymer electrolyte membrane fuel cells. Int J Hydrogen Energy 2024;51:1208–26.

[18] Mani SP, Kalaiyarasan M, Agilan P, Ravichandran K, Rajendran N, Meng Y. Evaluation of anticorrosion and contact resistance behavior of poly (orthophenylenediamine)- coated 316L SS bipolar plate for proton exchange membrane fuel cell. Int J Hydrogen Energy 2022;47:41097–110.

[19] Kumar A, Ricketts M, Hirano S. Ex situ evaluation of nanometer range gold coating on stainless steel substrate for automotive polymer electrolyte membrane fuel cell bipolar plate. J Power Sources 2010;195:1401–7.

[20] Mani SP, Agilan P, Kalaiarasan M, Ravichandran K, Rajendran N, Meng Y. Effect of multilayer CrN/CrAlN coating on the corrosion and contact resistance behavior of 316L SS bipolar plate for high temperature proton exchange membrane fuel cell. J Mater Sci Technol 2022;97:134–46.

[21] Mi BS, Chen Z, Wang Q, Li YFF, Qin ZW, Wang HB. Properties of C-doped CrTiN films on the 316L stainless steel bipolar plate for PEMFC. Int J Hydrogen Energy 2021;46:32645–54.

[22] Li W, Liu LT, Li ZX, Wang YF, Li HZ, Lei JJ. Corrosion and conductivity behavior of titanium-doped amorphous carbon film coated SS316L in the environment of PEMFCs. Mater Chem Phys 2022;276:125234.

[23] Gou Y, Chen H, Li R, Geng J, Shao Z. Nb–Cr–C coated titanium as bipolar plates for proton exchange membrane fuel cells. J Power Sources 2022;520:230797.

[24] Wang XZ, Zhang MM, Shi DD, Zhang SC, Wu YM, Gong WJ, et al. Long-term polarization accelerated degradation of nano-thin C/Ti coated SS316L bipolar plates used in polymer electrolyte membrane fuel cells. Int J Hydrogen Energy 2022;47:8974–92.

[25] Chang LQ, Luo XJ, Ding YY, Zhang JH, Gong XY, Zhong Y, et al. Improved corrosion resistance and interfacial conductivity of a-C/(Ti:C)/Ti nano-thin film for 316L stainless steel bipolar plates. Thin Solid Films 2024;794.

[26] Ma G, Yuan J, Chen R, Li H, Wu H, Yan J, et al. Balancing the corrosion resistance and conductivity of Cr-Al-C coatings via annealing treatment for metal bipolar plates. Appl Surf Sci 2022;597:153670.

[27] Ma GS, Zhang D, Guo P, Li H, Xin Y, Wang ZY, et al. Phase orientation improved the corrosion resistance and conductivity of Cr2AlC coatings for metal bipolar plates. J Mater Sci Technol 2022;105:36–44.

[28] ÖZkan D, Alper Yilmaz M, Szala M, TÜRkÜZ C, Chocyk D, TunÇ C, et al. Effects of ceramic-based CrN, TiN, and AlCrN interlayers on wear and friction behaviors of AlTiSiN+TiSiN PVD coatings. Ceram Int 2021.

[29] Bewilogua K, Hofmann D. History of diamond-like carbon films — from first experiments to worldwide applications. Surf Coating Technol 2014;242:214–25.

[30] Robertson J. Diamond-like amorphous carbon. Mater Sci Eng R Rep 2002;37: 129–281.

[31] Jin C, Guo P, Li H, Piao ZY, Komatsu K, Ma GS, et al. Temperature-relevant degradation in amorphous carbon coated SS316L bipolar plates for PEMFC. Surf Coating Technol 2024;484.

[32] Li H, Guo P, Zhang D, Liu LL, Wang ZY, Ma GS, et al. Interface-induced degradation of amorphous carbon films/stainless steel bipolar plates in proton exchange membrane fuel cells. J Power Sources 2020;469:228269.

[33] Li XB, Hou K, Qiu DK, Yi PY, Lai XM. A first principles and experimental study on the influence of nitrogen doping on the performance of amorphous carbon films for proton exchange membrane fuel cells. Carbon 2020;167:219–29.

[34] Wu B, Lin GQ, Fu Y, Hou M, Yi BL. Chromium-containing carbon film on stainless steel as bipolar plates for proton exchange membrane fuel cells. Int J Hydrogen Energy 2010;35:13255–61.

[35] Li X, Li L, Zhang D, Wang A. Ab initio study of interfacial structure transformation of amorphous carbon catalyzed by Ti, Cr, and W transition layers. ACS Appl Mater Interfaces 2017;9:41115–9.

[36] Préauchat B, Drawin S. Properties of PECVD-deposited thermal barrier coatings. Surf Coating Technol 2001;142–144:835–42.

[37] Li H, Xin Y, Komatsu K, Guo P, Ma G, Ke P, et al. Controlling the compactness and sp2 clusters to reduce interfacial damage of amorphous carbon/316L bipolar plates in PEMFCs. Int J Hydrogen Energy 2022.

[38] Li H, Guo P, Zhang D, Chen RD, Zuo X, Ke PL, et al. Influence of deposition temperature on the structure, optical and electrical properties of a-C films by DCMS. Appl Surf Sci 2020;503:144310.

[39] Mingge W, Congda L, Tao H, Guohai C, Donghui W, Haifeng Z, et al. Chromium interlayer amorphous carbon film for 304 stainless steel bipolar plate of proton exchange membrane fuel cell. Surf Coating Technol 2016;307:374–81.

[40] Mingge W, Congda L, Dapeng T, Tao H, Guohai C, Donghui W. Effects of metal buffer layer for amorphous carbon film of 304 stainless steel bipolar plate. Thin Solid Films 2016;616:507–14.

[41] Konkhunthot N, Tunmee S, Zhou XL, Komatsu K, Photongkam P, Saitoh H, et al. The correlation between optical and mechanical properties of amorphous diamond-like carbon films prepared by pulsed filtered cathodic vacuum arc deposition. Thin Solid Films 2018;653:317–25.

[42] Kishimoto S, Hashiguchi T, Ohshio S, Saitoh H. Density investigation by X-ray reflectivity for thin films synthesized using atmospheric CVD. Chem Vap Depos 2008;14:303–8.

[43] Parratt LG. Surface studies of solids by total reflection of X-rays. Phys Rev 1954;95: 359–69.

[44] Husby H, Kongstein OA, Oedegaard A, Seland F. Carbon-polymer composite coatings for PEM fuel cell bipolar plates. Int J Hydrogen Energy 2014;39:951–7.

[45] Wang Y, Northwood DO. An investigation of the electrochemical properties of PVD TiN-coated SS410 in simulated PEM fuel cell environments. Int J Hydrogen Energy 2007;32:895–902.

[46] Wang Y, Northwood DO. Effects of O2 and H2 on the corrosion of SS316L metallic bipolar plate materials in simulated anode and cathode environments of PEM fuel cells. Electrochim Acta 2007;52:6793–8.

[47] Antunes RA, Oliveira MCL, Ett G, Ett V. Corrosion of metal bipolar plates for PEM fuel cells: a review. Int J Hydrogen Energy 2010;35:3632–47.

[48] Davies DP, Adcock PL, Turpin M, Rowen SJ. Bipolar plate materials for solid polymer fuel cells. J Appl Electrochem 2000;30:101–5.

[49] Li HC, Li XW, Wei J, Wang ZY, Guo P, Ke PL, et al. Crystalline transformation from ta-C to graphene induced by a catalytic Ni layer during annealing. Diam Relat Mater 2020;101:107556.

[50] Li L, Liu LL, Li X, Guo P, Ke P, Wang A. Enhanced tribocorrosion performance of Cr/GLC multilayered films for marine protective application. ACS Appl Mater Interfaces 2018;10:13187–98.

[51] Li L, Guo P, Liu LL, Li XW, Ke PL, Wang AY. Structural design of Cr/GLC films for high tribological performance in artificial seawater: Cr/GLC ratio and multilayer structure. J Mater Sci Technol 2018;34:1273–80.

[52] Ferrari AC, Robertson J. Interpretation of Raman spectra of disordered and amorphous carbon. Phys Rev B 2000;61:14095–107.

[53] Tuinstra F, Koenig JL. Raman spectrum of graphite. J Chem Phys 1970;53: 1126–30.

[54] Chu PK, Li LH. Characterization of amorphous and nanocrystalline carbon films. Mater Chem Phys 2006;96:253–77.

[55] Wei J, Guo P, Liu L, Li H, Li H, Wang S, et al. Corrosion resistance of amorphous carbon film in 3.5 wt% NaCl solution for marine application. Electrochim Acta 2020;346:136282.

[56] Xie J, Komvopoulos K. The effect of Argon ion irradiation on the thickness and structure of ultrathin amorphous carbon films. J Appl Phys 2016;119:095304.

[57] Cuomo JJ, Doyle JP, Bruley J, Liu JC. Sputter deposition of dense diamond-like carbon films at low temperature. Appl Phys Lett 1991;58:466–8.

[58] Liu L, Wang T, Huang JL, He ZB, Yi Y, Du K. Diamond-like carbon thin films with high density and low internal stress deposited by coupling DC/RF magnetron sputtering. Diam Relat Mater 2016;70:151–8.

[59] Ferrari AC, Li Bassi A, Tanner BK, Stolojan V, Yuan J, Brown LM, et al. Density, sp (3) fraction, and cross-sectional structure of amorphous carbon films determined by x-ray reflectivity and electron energy-loss spectroscopy. Phys Rev B 2000;62: 11089–103.

[60] Zhang Q, Yoon SF, Ahn RJ, Yang H, Bahr D. Deposition of hydrogenated diamond-like carbon films under the impact of energetic hydrocarbon ions. J Appl Phys 1998;84:5538–42.

[61] Ioka I, Yoda S. Measurements of the density profile in oxidized graphite by X-ray computed-tomography. J Nucl Mater 1988;151:202–8.

[62] Olsson COA, Landolt D. Passive films on stainless steels—chemistry, structure and growth. Electrochim Acta 2003;48:1093–104.

[63] Yi P, Zhang W, Bi F, Peng L, Lai X. Enhanced corrosion resistance and interfacial conductivity of TiC x/a-C nanolayered coatings via synergy of substrate bias voltage for bipolar plates applications in PEMFCs. ACS Appl Mater Interfaces 2018; 10:19087–96.

[64] Yi P, Zhang D, Peng L, Lai X. Impact of film thickness on defects and the graphitization of nanothin carbon coatings used for metallic bipolar plates in proton exchange membrane fuel cells. ACS Appl Mater Interfaces 2018;10: 34561–72.

[65] Wang ZY, Feng K, Li ZG, Lu FG, Huang J, Wu YX, et al. Self-passivating carbon film as bipolar plate protective coating in polymer electrolyte membrane fuel cell. Int J Hydrogen Energy 2016;41:5783–92.

[66] Khakzadian J, Hosseini SH, Zangeneh Madar K. The effect of the substrate temperature on the microstructure properties of the NiCrAl coating in cathodic arc deposition. Surf Coating Technol 2018;337:342–8.